

Applications of the chiral potential with the semi-local regularization in momentum space to the disintegration processes

V. Urbanevych, R. Skibiński, H. Witała, J. Gólak, K. Topolnicki, and A. Grassi

*M. Smoluchowski Institute of Physics,
Jagiellonian University, PL-30348 Kraków, Poland*

E. Epelbaum and H. Krebs

*Ruhr-Universität Bochum, Fakultät für Physik und Astronomie,
Institut für Theoretische Physik II, D-44780 Bochum, Germany*

(Dated: July 30, 2020)

Abstract

We apply the chiral potential with the momentum space semi-local regularization to the ^2H and ^3He photodisintegration processes and to the (anti)neutrino induced deuteron breakup reactions. Specifically, the differential cross section, the photon analyzing power and the final proton polarization have been calculated for the deuteron photodisintegration at the photon energies 30 MeV and 100 MeV. For the ^3He photodisintegration predictions for the semi-inclusive and exclusive differential cross sections are presented for the photon energies up to 120 MeV. The total cross section is calculated for the (anti)neutrino disintegrations of the deuteron for the (anti)neutrino energies below 200 MeV. The predictions based on the Argonne V18 potential or on the older chiral force with regularization applied in coordinate space are used for comparison. Using the fifth order chiral nucleon-nucleon potential supplemented with dominant contributions from the sixth order allows us to obtain converged predictions for the regarded reactions and observables. Our results based on the newest semi-local chiral potentials show even smaller cutoff dependence for the considered electroweak observables than the previously reported ones with a coordinate-space regulator. However, some of the studied polarization observables in the deuteron photodisintegration process reveal more sensitivity to the regulator value than the unpolarized cross section. The chiral potential regularized semi-locally in momentum space yields also fast convergence of results with the chiral order. These features make the used potential a high quality tool to study electroweak processes.

PACS numbers: 13.75.Cs, 21.45.-v, 25.10.+s, 25.20.x, 13.15.+g

I. INTRODUCTION

Chiral effective field theory (χ EFT) is nowadays the most reliable approach to study low-energy nuclear forces. It's continuous development for nearly 30 years resulted in advanced two-nucleon and many-nucleon interactions [1–7].

In 2018 the Bochum group presented a new version of the chiral interaction [1], which differs from the previous realization, among others, by the regularization scheme applied directly in momentum space. This semi-local momentum-space (SMS) regularized potential has been derived completely up to the fifth order (N^4 LO) of the chiral expansion and some contributions from the sixth order have been even included in its “ N^4 LO⁺” version. Up to now this potential has been used out of necessity in the two-nucleon (2N) system to fix its free parameters and later applied to nucleon-deuteron elastic scattering as well as to the nucleon induced deuteron breakup process [8, 9], delivering at the N^2 LO a data description of the similar quality as the non-chiral semi-phenomenological potentials. In this paper we extend applications of the SMS interaction beyond the purely strong processes to a few electroweak reactions.

Investigations of the electroweak processes with the older chiral force with the non-local regularization resulted in predictions strongly dependent on the cut-off parameter (see e.g. [10–12]). Such a picture was observed with the single-nucleon current and with inclusion of some meson-exchange currents. In 2016 we showed [13] that semi-local regularization (applied in coordinate space) helps to avoid such big variations with respect to the regulator, but predictions were still clearly dependent on the cutoff parameter. In the present paper we check if properties of the SMS potential match or possibly even surpass those of the former version of the chiral potential. To this end we apply the SMS chiral potential to the selected electromagnetic and weak processes. Specifically we study the $\gamma + ^2\text{H} \rightarrow \text{p} + \text{n}$, $\nu_e + ^2\text{H} \rightarrow \nu_e + \text{p} + \text{n}$, $\bar{\nu}_e + ^2\text{H} \rightarrow \bar{\nu}_e + \text{p} + \text{n}$, $\bar{\nu}_e + ^2\text{H} \rightarrow e^+ + \text{n} + \text{n}$ and $\gamma + ^3\text{He} \rightarrow \text{p} + \text{p} + \text{n}$ reactions. For the sake of comparison we also use the results of our previous research with the semi-local coordinate-space (SCS) regularized potential [5, 14] and with the Argonne V18 (AV18) potential [15].

One of the most challenging problems with the application of a nucleon-nucleon (NN) potential to electroweak processes with nuclear systems is a construction of consistent two-nucleon (2N) and, more generally, many-nucleon electroweak current operators [16].

Many-nucleon currents linked to various models of nuclear forces have been investigated for a long time (see e.g. [17–23]). No full 2N electromagnetic or weak current operator consistent with the SMS chiral force has been derived yet, see however [24] for the recent calculation of the deuteron structure radius with the consistent 2N charge operator. Thus we rely on the single-nucleon current (SNC) and use the Siegert theorem to take into account many-body contributions to the nuclear electromagnetic current. Many-nucleon currents, even included implicitly, are absolutely indispensable in a correct treatment of photonuclear reactions. It has been shown (see for example Ref. [25]) that their omission leads to incorrect predictions, especially for polarization observables. In the case of weak reactions we use the non-relativistic form of the single-nucleon weak current operator, whose components are defined in Ref. [26]. The dominant role of the single-nucleon weak current in neutrino scattering of the deuteron has been recently demonstrated by Baroni and Schiavilla [23] who have found only a few percent contribution from higher order current operators.

The rest of this paper is structured as follows. In the next section we briefly describe our formalism and then in Sec. III we show our results for the deuteron photodisintegration

and (anti)neutrino induced deuteron disintegration processes. Section IV comprises our predictions for ${}^3\text{He}$ disintegration. We summarize and conclude in Sec. V.

II. THEORETICAL FORMALISM

Our approach, which is based on the Schrödinger and Lippmann-Schwinger equations (for 2N reactions) and on the Faddeev formalism (for 3N reactions) has been described in detail in [25–27]. In short, the path to the observables for the electromagnetic or weak disintegrations leads through the appropriate nuclear matrix elements.

For the deuteron photodisintegration process, in the nuclear matrix elements

$$N_{deu}^\mu \equiv \langle \Psi_{scatt}^{2N} | j_{2N}^\mu | \Psi_{bound}^{2N} \rangle, \quad (2.1)$$

a full 2N electromagnetic current operator appears between the initial deuteron bound state $|\Psi_{bound}^{2N}\rangle$ and the final 2N scattering state $|\Psi_{scatt}^{2N}\rangle$. In order to obtain the deuteron bound state we solve the Schrödinger equation with a given 2N potential V . Further, the scattering state is constructed from a solution of the Lippmann-Schwinger equation for the t operator: $t = V + tG_0V$, where G_0 is a free 2N propagator. Using this equation (2.1) takes the form:

$$N_{deu}^\mu = \langle \vec{p}_0 | (1 + tG_0)j_{2N}^\mu | \Psi_{bound}^{2N} \rangle, \quad (2.2)$$

where $|\vec{p}_0\rangle$ is the antisymmetrized eigenstate of the relative proton-neutron momentum.

Our formalism for the (anti)neutrino induced deuteron disintegrations is essentially the same [26, 28, 29]. Especially, for the neutral-current (NC) driven processes the isospin structure of the current operator and the 2N final state are the same as for the photodisintegration reaction. In the case of the charged-current (CC) driven reaction only some straightforward modifications are introduced in the corresponding weak single-nucleon current operator.

For the ${}^3\text{He}$ photodisintegration with three free nucleons in the final state, if the 3N force is neglected, the nuclear matrix elements are given as [25]:

$$N_{3N}^\mu = \langle \Phi_{3N} | (1 + P)j_{3N}^\mu | \Psi_{bound}^{3N} \rangle + \langle \Phi_{3N} | (1 + P) | U^\mu \rangle, \quad (2.3)$$

where $|\Psi_{bound}^{3N}\rangle$ represents the initial 3N bound state and $|\Phi_{3N}\rangle$ is an antisymmetrized state which describes the free motion of three outgoing nucleons. Further, the permutation operator P is built from transpositions P_{ij} of particles i and j : $P = P_{12}P_{23} + P_{13}P_{23}$ and the auxiliary state $|U^\mu\rangle$ allows us to include all the final state interactions among the three outgoing nucleons. It is a solution of the Faddeev-like equation [25] which reads

$$|U^\mu\rangle = t\tilde{G}_0(1 + P)j_{3N}^\mu | \Psi_{bound}^{3N} \rangle + t\tilde{G}_0P|U^\mu\rangle, \quad (2.4)$$

where \tilde{G}_0 is a free 3N propagator and j_{3N}^μ is the total 3N electromagnetic current operator.

At the moment 2N currents, with the same regularization as used in the SMS interaction investigated here, are not available. While their operator form has been already derived [22, 30–34], a consistent regularization of these currents is still under development. Thus for the weak processes we use contributions from the single-nucleon currents only. In the case of the electromagnetic reactions additional contributions are taken implicitly into account using the Siegert theorem, as described in detail in Ref. [12, 25, 27]. We partly substitute electric multipoles by the Coulomb ones, calculated from the single-nucleon charge density

operator. To this end we carry out the multipole decomposition of the corresponding SNC matrix elements.

We perform our calculations in the momentum space, in the partial wave decomposition scheme. For the deuteron disintegration we take into account all partial waves in the 2N system up to the total angular momentum $j = 4$. For ${}^3\text{He}$ photodisintegrations we use all two-nucleon partial waves up to the total 2N angular momentum $j = 3$ and all three-nucleon partial waves up to the total 3N angular momentum $J = \frac{15}{2}$. For further details on our computational scheme see Ref. [25].

III. RESULTS FOR ${}^2\text{H}$ DISINTEGRATION

First we discuss our results for the deuteron photodisintegration process $\gamma + {}^2\text{H} \rightarrow \text{p} + \text{n}$ at two laboratory photon energies $E_\gamma = 30$ MeV and $E_\gamma = 100$ MeV. Figure 1 shows the differential cross section $\frac{d^2\sigma}{d\Omega}$ obtained using the chiral SMS potential for both energies. For the sake of comparison we also show predictions obtained using the AV18 NN potential [15]. Both for the chiral SMS force and for the AV18 potential our predictions were obtained with the single-nucleon current supplemented implicitly by some 2N parts, using the Siegert theorem [10].

In the left column of Fig.1 we present results calculated at different chiral orders (from LO to N^4LO^+) with the regularization parameter $\Lambda = 450$ MeV. For the energy $E_\gamma = 30$ MeV (top row) only the LO prediction is noticeably separated from all others and the difference among remaining predictions is very small ($\approx 0.06\%$ at the maximum of the cross section between N^2LO and N^3LO results) and even less for all subsequent chiral orders. It shows that for this photon energy the SMS potential based predictions converge rapidly and contributions from high orders are not crucial. At 100 MeV our predictions converge more slowly, but starting from N^2LO all the curves are very close to each other (the difference between the lines remains below 3%). In the case of $E_\gamma = 100$ MeV the data description is worse than at $E_\gamma = 30$ MeV, but based on the semi-phenomenological results by Arenhövel *et al.* [35] it is expected that for higher energies 2N electromagnetic currents contribute substantially and we thus expect that our predictions will improve significantly when explicit 2N current operators, fully consistent with the 2N potential, are included.

The middle column of Fig.1 presents the truncation errors arising, at a given chiral order, due to neglecting of higher-order contributions to the chiral potential. These theoretical estimates were calculated employing the prescription advocated in [36] and later used also for electromagnetic reactions with the SCS potential in [13]¹. The observed picture demonstrates that only tiny contributions from the potential components above N^4LO should be expected, as the band showing the truncation error for the highest presented chiral order N^4LO^+ is quite narrow - its width in the maximum of the cross section is around 0.1% (2.5%) of the cross section magnitude at the photon energy $E_\gamma = 30$ MeV (100 MeV). Notice, however, that the estimates of truncation error may change upon performing a more complete treatment of the current operators.

Finally, the right column of Fig.1 shows the dependence of predictions on the value of the regularization parameter Λ in the range $\Lambda \in [400, 550]$ MeV. It is clearly seen that the SMS potential provides us with a weak dependence of the predicted cross section on the cut-off

¹ It is also possible to perform a more sophisticated estimation based on the Bayesian approach [8, 37], however, for the sake of comparison with [13] we use the prescription [36] in this work.

parameter at both investigated energies. This is an important improvement compared to the older versions of the chiral force (see e.g. [13]), where regularization strongly influenced the results, yielding a spread of predictions up to 20% for small proton scattering angles at $E_\gamma = 100$ MeV.

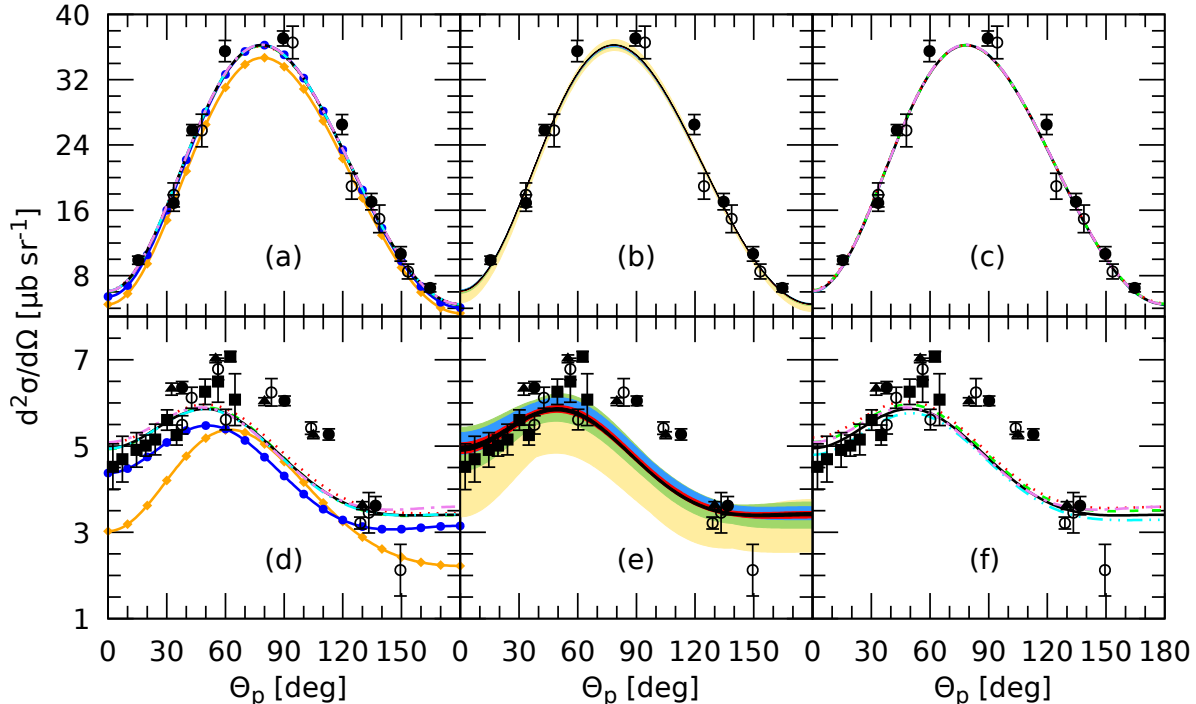


FIG. 1. The differential cross section $\frac{d^2\sigma}{d\Omega}$ for the $\gamma + {}^2\text{H} \rightarrow \text{p} + \text{n}$ reaction at the laboratory photon energy $E_\gamma = 30$ MeV (top) and $E_\gamma = 100$ MeV (bottom) as a function of the proton emission angle θ_p (the angle between the initial photon momentum and the proton momentum) in the center of mass frame. The left column shows the dependence of predictions on the order of chiral expansion. The orange solid line with diamonds, the blue solid line with circles, the green dashed, the red dotted, the black solid, the cyan double-dot-dashed and the violet dot-dashed curves correspond to the LO, NLO, N^2LO , N^3LO , N^4LO , $\text{N}^4\text{LO}+$ and AV18 potential based predictions, respectively. Truncation errors for the different orders of chiral expansion are presented in the middle column. The yellow band shows the truncation errors at the NLO, green - at the N^2LO , blue - at the N^3LO , red - at the N^4LO and black one at the $\text{N}^4\text{LO}+$ orders. The right column shows the chiral SMS predictions at N^4LO , calculated using different values of the cut-off parameter Λ . The cyan double-dot-dashed, the black solid, the green dashed, the red dotted and the violet dot-dashed curves correspond to $\Lambda = 400$ MeV, 450 MeV, 500 MeV, 550 MeV, and to the AV18 based predictions respectively. For the predictions shown in the left and in the middle columns the regulator value $\Lambda = 450$ MeV is used. The data points at 30 MeV are the same as in [38] and at 100 MeV are taken from [38] (open and filled circles, squares) and from [39] (triangles).

Our previous investigations [13] were devoted to the application of the older version of the NN potential, namely the chiral SCS force, to some electroweak processes. In particular, this potential applied to the deuteron photodisintegration reaction yields predictions for the

differential cross section well converged with respect to the order of chiral expansion. Now we are in a position to compare the outcomes from the SMS and from the SCS potentials. Results of our calculations of the differential cross section obtained using higher chiral orders (starting from N³LO) of these two forces are presented in Figs. 2 and 3 for the photon energy 30 MeV and 100 MeV, respectively. It is interesting that despite the convergence of both potentials, curves approach different values of the cross section and quite a big gap between predictions of the SMS and SCS potentials is visible on both figures including the inset in Fig. 2. The difference between the N⁴LO SMS and SCS cross sections at $E_\gamma = 30$ MeV reaches $1.07 \mu\text{b sr}^{-1}$ ($\approx 3\%$) at $\theta_p = 79^\circ$ and $0.467 \mu\text{b sr}^{-1}$ ($\approx 8\%$) at $\theta_p = 52^\circ$ for $E_\gamma = 100$ MeV. The observed deviation can be caused by the fact that the potentials use different values of low energy constants, which results also in different deuteron wave functions. It is also possible that the lack of explicit 2N current contributions affects differently the predictions based on the two potentials. Absence of such gaps for full calculations, that is ones including an electromagnetic current, which is complete and consistent with the NN interaction, will be a challenging test for the chiral approach.

It is also worth mentioning that one has to be cautious about judging the agreement between predictions obtained with the two potentials as, beside the various regularization schemes, they differ in other aspects [1]. Even regarding the regularization method itself it is not possible to establish any one to one correspondence between particular values of regulators in the two spaces. The prescription given in Ref. [40], $\frac{2}{R} \leftrightarrow \Lambda$, yields $\Lambda \approx 438$ MeV for $R = 0.9$ fm. It means that $\Lambda = 450$ MeV and $R = 0.9$ fm deliver only approximately the same regularization effect.

Nevertheless, since for the SMS potential its version for $\Lambda = 450$ MeV is available, here and in other cases where results based on the two potentials are compared, we use the accessible pair of regulators: $R = 0.9$ fm and $\Lambda = 450$ MeV. For the presented here calculations the comparison with experimental data cannot be used to judge between both forces because depending on the photon energy or the proton scattering angle either one or the other prediction is closer to the data. Moreover, the inclusion of consistent two-body currents may change predictions differently for both interactions.

In Figs. 4 and 5 we compare predictions based on the two chiral potentials, SMS and SCS, more closely. We show the relative difference between the differential cross section for all the presented chiral orders. To this end, we define $\delta\sigma(\text{chiral order})$ as a difference between the maximum and minimum values of $\frac{d^2\sigma}{d\Omega}$ among predictions at orders from LO to N⁴LO(N⁴LO⁺) for the SCS(SMS) forces for each angle θ_p and divide it by the mean value from five(six) predictions for the SCS(SMS), correspondingly. The resulting quantity both for the SMS (solid green line) and the SCS (dashed violet line) potentials is presented as a function of the proton detection angle in the left panels of Fig. 4 for $E_\gamma = 30$ MeV, and Fig. 5 for $E_\gamma = 100$ MeV. In both cases the SCS result lies above the SMS one which means that the net spread with respect to chiral orders for the newer potential is smaller. Nevertheless this observation can also be an effect of the leading order predictions, which for the SMS as well as for the SCS case are far away from all the other results. Therefore it is interesting to check the absolute difference between differential cross sections at N³LO and N⁴LO for the two potentials, which is done in Figs. 4c and 5c. One can see that on both plots the SMS prediction is above the SCS one for nearly all scattering angles. Thus the contribution from N⁴LO is bigger for the new SMS potential.

Figures 4b and 5b show $\delta\sigma(\Lambda)$, which is an analogous quantity to this shown in Figs. 4a and 5a, but now defined with respect to the values of the regularization parameter. That

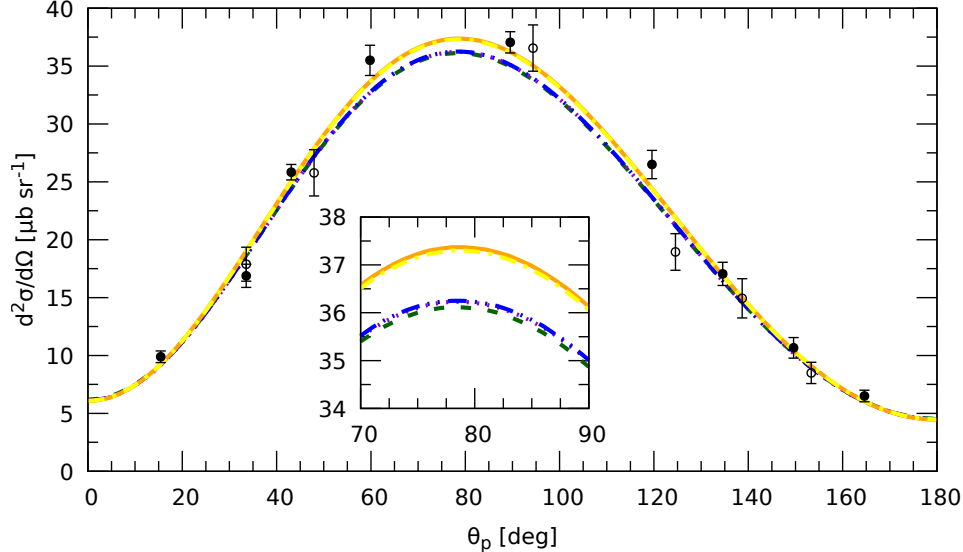


FIG. 2. The differential cross section $\frac{d^2\sigma}{d\Omega}$ at $E_\gamma = 30$ MeV as a function of the proton emission angle θ_p calculated using the SCS (with $R = 0.9$ fm) and the SMS (with $\Lambda = 450$ MeV) chiral potentials at higher orders of chiral expansion (N^3 LO, N^4 LO and N^4 LO+ (for the SMS force only)). The green dashed, violet dotted and blue double-dot-dashed lines represent results calculated using the SMS potential up to N^3 LO, N^4 LO and N^4 LO+ respectively. The orange solid and the yellow dash-dotted lines are obtained using the SCS potential at N^3 LO and N^4 LO, respectively. All data points (open and filled circles) are taken from [38].

means that $\delta\sigma(\Lambda)$ is the difference between the largest and the smallest value of $\frac{d^2\sigma}{d\Omega}$, calculated using all values of the cut-off parameter (R for the SCS and Λ for the SMS) divided by its average $\sigma_{avg(\Lambda)}$. From the figure it is clear that dependence on the cut-off parameter is much weaker for the new potential. Note that for the SCS interaction, which comprises also softer regulators, like $R=1.2$ fm, some artifacts may be introduced to the potential, leading to a wider spread of the predictions.

Figure 6 demonstrates convergence of the cross section with respect to the chiral order. Each of the panels represents a certain combination of the photon energy and the proton emission angle: $E_\gamma = 30$ MeV, $\theta_p = 60^\circ$ at Fig. 6a, $E_\gamma = 100$ MeV, $\theta_p = 15^\circ$ at Fig. 6b, and $E_\gamma = 100$ MeV, $\theta_p = 150^\circ$ at Fig. 6c. The quantity presented in this figure is the absolute difference between differential cross section $\frac{d^2\sigma}{d\Omega}$ at each two subsequent orders: the one given by the corresponding value on the x -axis and the subsequent one. For example the value with x -coordinate NLO is nothing but $\left| \frac{d^2\sigma}{d\Omega} \Big|_{N^2LO} - \frac{d^2\sigma}{d\Omega} \Big|_{NLO} \right|$. We see that the SCS potential tends to converge faster, at least at presented scattering angles, since the difference shown in Fig. 6 drops to zero earlier. This is in agreement with the results shown in Fig. 4c. Nevertheless the presence of an additional term N^4 LO+ in the SMS potential makes the SMS predictions converge as well, though with more terms included. The SMS potential does not reveal a jump between N^2 LO and N^3 LO predictions as observed for the SCS force, what is caused by different off-shell behaviour of the potential. Again, as in the case of the comparison with data, it would be interesting to see the convergence pattern for the

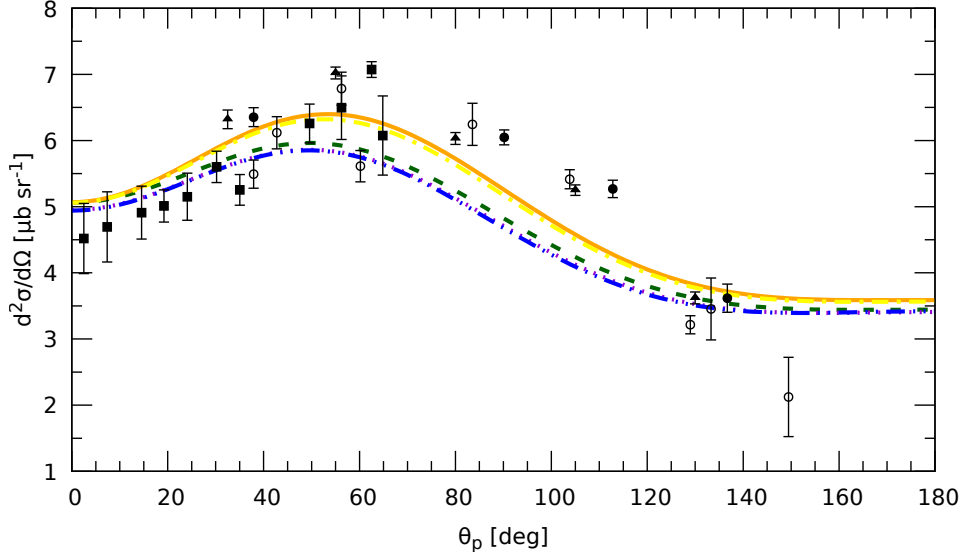


FIG. 3. The same as in Fig. 2 but for $E_\gamma = 100$ MeV. Data are taken from [39] (triangles) and from [38] (open and filled circles and squares).

predictions obtained with complete currents for both potentials.

In Figs. 7 and 8 we give examples of the SMS chiral force predictions for the polarization observables in the deuteron photodisintegration process [35]. Figure 7 presents the photon analyzing power A_X as a function of the outgoing proton angle θ_p at the photon laboratory energy $E_\gamma = 100$ MeV. Figure 7a shows the dependence of predictions on the order of the chiral expansion with a fixed regulator $\Lambda = 450$ MeV. One can see that few lowest orders of expansion are not sufficient to obtain convergence of the predictions, as only after N³LO lines overlap. This can indicate that subsequent orders do not bring significant contributions to the observable's final value. In Fig. 7b each curve corresponds to the particular value of Λ (taken as 400 MeV, 450 MeV, 500 MeV, and 550 MeV) used in N⁴LO calculations. It is clearly visible that for A_X the dependence on the regulator value is much stronger than for the maximum of the differential cross section (Fig.1) and amounts up to 14%, so in this case a proper choice of the Λ parameter value can be important in order to obtain realistic predictions. In Fig. 8 we present the outgoing proton polarization P_y for the same reaction. The dependence of the predictions on the Λ value is slightly weaker for P_y than for A_X , since at the minimal values of these observables the relative difference between predictions with different regulator values is less than 5% for P_y (at $\theta_p = 131^\circ$) and reaches nearly 14% for A_X (at $\theta_p = 72^\circ$). All our predictions for the deuteron photodisintegration are in a good agreement with the results obtained using the AV18 force and the observed differences amount to approximately 12% (7%) for A_X (P_y) at the minima.

Now we turn to the neutrino and antineutrino induced deuteron disintegration processes. For obvious reasons we restrict ourselves to the total cross sections σ_{tot} . These results are obtained from the nuclear response functions generated on dense rectilinear grids of the (E_{2N}, Q) points, where E_{2N} is the internal 2N energy and Q is the magnitude of the three-momentum transfer [29]. Figure 9 presents predictions for the total cross section σ_{tot} for the $\nu_e + {}^2\text{H} \rightarrow \nu_e + p + n$ neutral-current driven reaction. Again, in the left panel we show

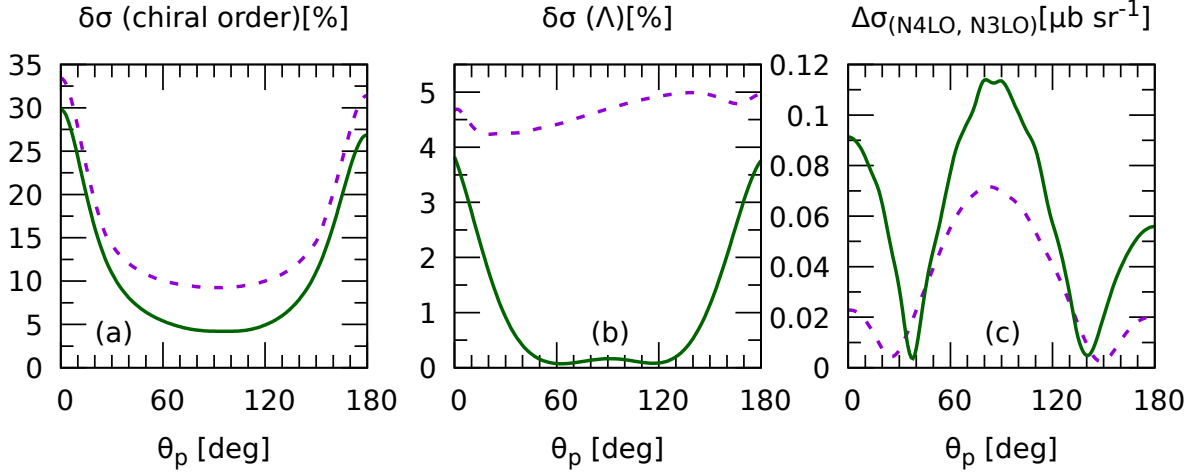


FIG. 4. The relative spread of predictions for the differential cross section for the deuteron photodisintegration reaction at the initial photon energy $E_\gamma = 30$ MeV. Left panel (a) represents the difference between maximum and minimum values of the differential cross section for all chiral orders used, divided by its average (from LO to $N^4\text{LO}^+$ for the SMS potential - green solid line, and from LO to $N^4\text{LO}$ for the SCS - violet dashed line). The middle panel (b) shows analogous quantity, but measuring the spread with respect to the different cutoff values used (from 400 MeV to 550 MeV for the SMS force and from 0.8 to 1.2 fm for the SCS potential) at fixed chiral order ($N^4\text{LO}$). The right panel (c) shows absolute difference between $\frac{d^2\sigma}{d\Omega}$ calculated at $N^4\text{LO}$ and $N^3\text{LO}$ for each of two potentials.

results obtained using different orders of the chiral expansion (from LO up to $N^4\text{LO}^+$, $\Lambda=450$ MeV) and in Fig. 9b the variation of the results with respect to the cutoff parameter value is presented. For the sake of comparison with the results based on a semi-phenomenological potential we also give predictions based on the AV18 interaction. The same dependencies but for the antineutrino induced NC disintegration $\bar{\nu}_e + {}^2\text{H} \rightarrow \bar{\nu}_e + p + n$ are presented in Fig. 10. The results for the charged-current induced process $\bar{\nu}_e + {}^2\text{H} \rightarrow e^+ + n + n$ are demonstrated in Fig. 11.

As for our energy range σ_{tot} takes a large spectrum of values, it is hard to see the differences between curves in Figs. 9, 10 and 11 with the naked eye. However, in the insets one can see that in the left panels of Figs. 9, 10 and 11 the two curves, representing the LO and the AV18 predictions, are separated from all the others. It is interesting that the relative position of the different curves in the inset in Fig. 11a does not remain the same trough all the energy range. It is so for $E_\gamma \in (0, 145)$ MeV and then the LO curve swaps position with the NLO one, which gives the biggest predictions at the higher energies.

In the right panels of Figs. 9-11 there are results of our calculations at $N^4\text{LO}$ using different regulator values. To give some numerical examples: for the initial particle energy $E_{\nu(\bar{\nu})}=100$ MeV the relative differences between values of total cross section σ_{tot} calculated with the chiral SMS force up to the fifth order ($N^4\text{LO}$) and up to fifth order plus corrections from the sixth order ($N^4\text{LO}^+$) are 0.093% for $\nu_e + {}^2\text{H} \rightarrow \nu_e + p + n$, 0.092% for $\bar{\nu}_e + {}^2\text{H} \rightarrow \bar{\nu}_e + p + n$ and 0.029% for the $\bar{\nu}_e + {}^2\text{H} \rightarrow e^+ + n + n$ reactions. The relative differences for the cross section obtained using different values of the cut-off parameter at the same

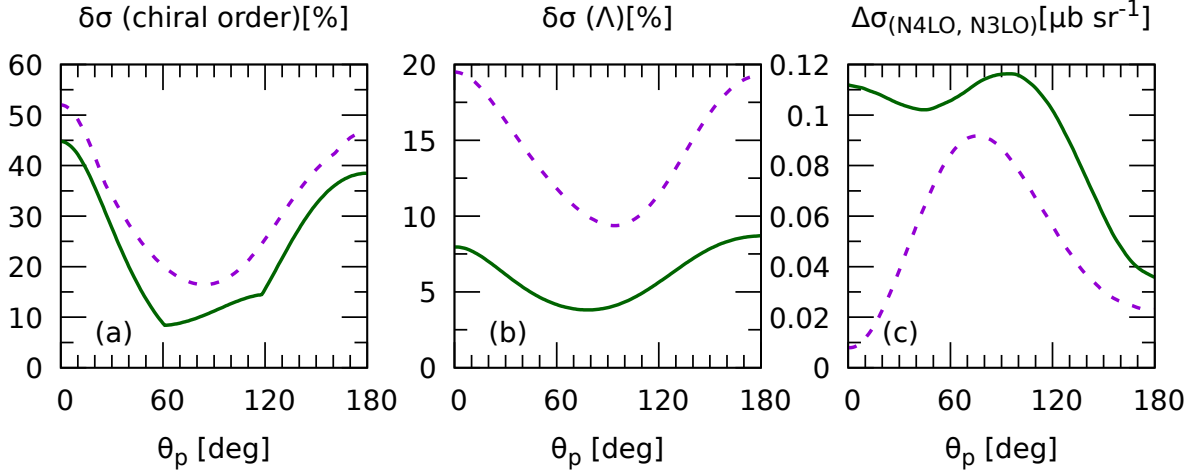


FIG. 5. Same as in Fig. 4 but for $E_\gamma = 100$ MeV.

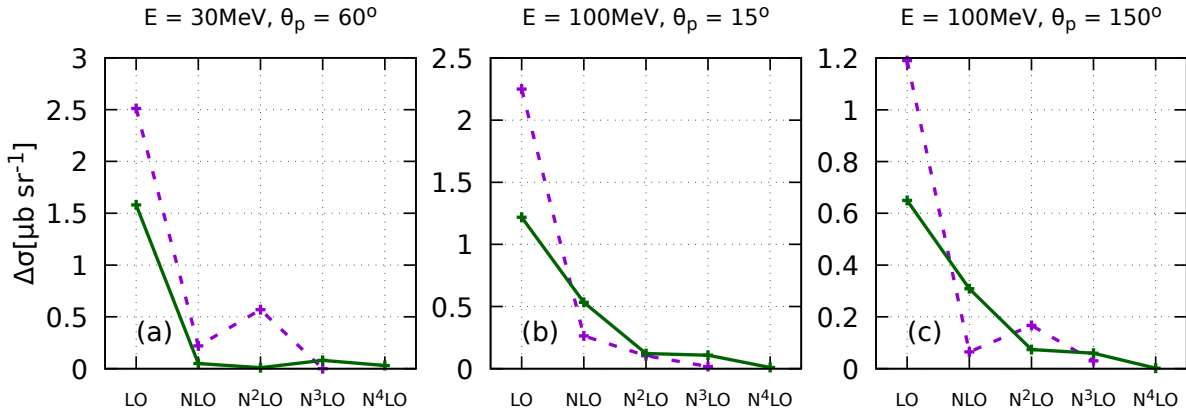


FIG. 6. The absolute difference between the values of the differential cross section $\frac{d^2\sigma}{d\Omega}$ taken at each two subsequent chiral orders (the one marked on the x-axis and the next one) at fixed proton angle θ_p and photon energy: $\theta_p = 60^\circ$ $E_\gamma = 30$ MeV(a), $\theta_p = 15^\circ$ $E_\gamma = 100$ MeV(b), $\theta_p = 150^\circ$ $E_\gamma = 100$ MeV(c). The violet dashed (the green solid) line represents results obtained using the SCS (SMS) potential with the cutoff parameter $R = 0.9$ fm ($\Lambda = 450$ MeV).

energy, at $N^4\text{LO}$, are 0.96%, 0.98% and 0.90% for the same reactions, respectively. It is seen that the cutoff dependence is nearly one order bigger than difference between the last two chiral orders. Nevertheless both uncertainties remain very small which reflects low sensitivity of these inclusive observables to employed dynamics. The relative difference of $N^4\text{LO}$ and $N^4\text{LO}^+$ predictions for the last reaction is approximately three times smaller than for the first two in both regarded cases. Our treatment of all above mentioned weak reactions is very similar. The common ingredients are the deuteron wave functions and the kinematics, which is only slightly modified due to the small but non-zero positron mass. The single-nucleon weak neutral and charged currents are potential independent so they

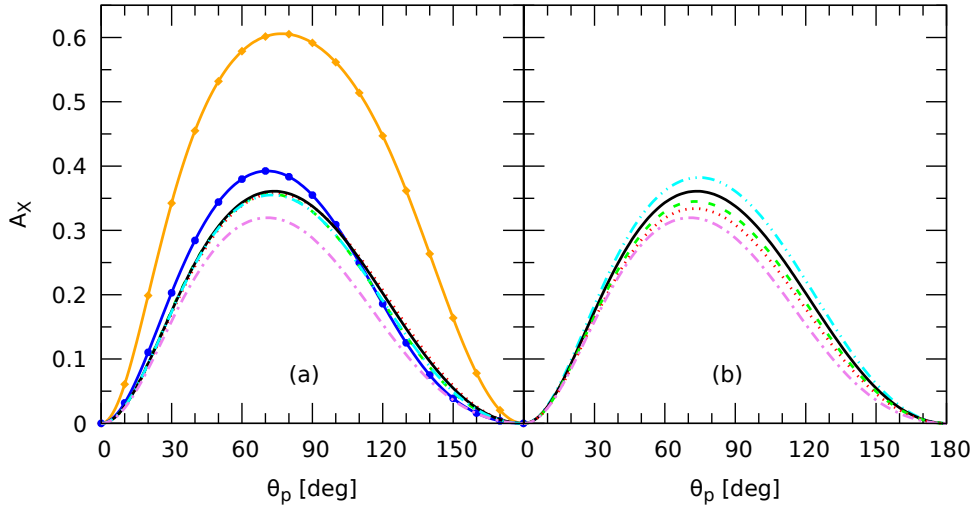


FIG. 7. The photon analyzing power A_X as a function of the center-of-mass proton detection angle θ_p for the deuteron photodisintegration process at $E_\gamma = 100$ MeV. The left panel (a) shows the dependence of A_X on the chiral order of the SMS potential at $\Lambda=450$ MeV. The right panel demonstrates the dependence of A_X on the value of the cutoff parameter Λ at $N^4\text{LO}$. Lines are as in Figs. 1a and 1c, respectively.

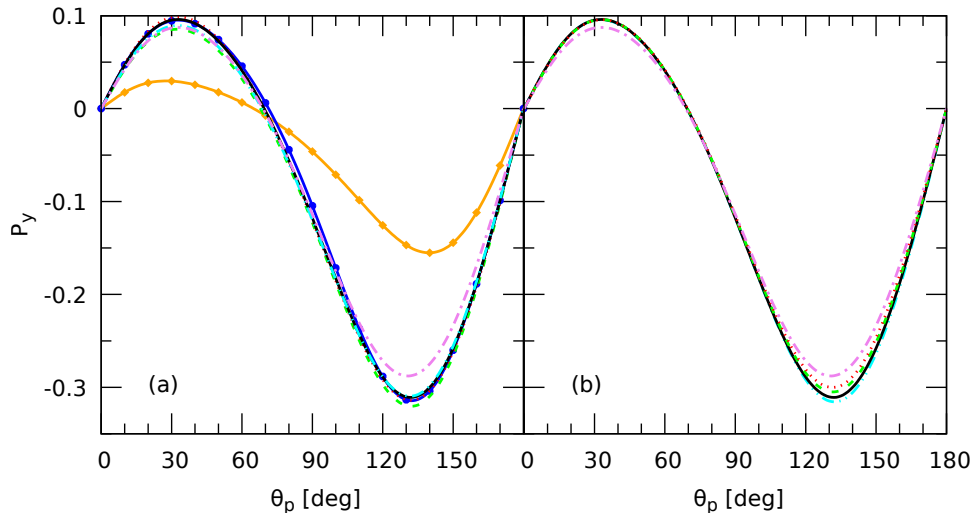


FIG. 8. Same as in Fig. 7 but for the proton polarization P_y .

cannot explain the difference in $N^4\text{LO} - N^4\text{LO}^+$ spreads for the NC and CC driven reactions. However, the final states for the reactions are different. While in the first two reactions driven by the neutral current a neutron-proton pair emerges in the final state, in the third process, $\bar{\nu}_e + {}^2\text{H} \rightarrow e^+ + n + n$, a two-neutron final state is present. Thus the observed variation in spreads stems from the difference between the neutron-neutron and neutron-proton potentials. From Figs. 9-11 it is visible that AV18 curve here is also detached

from all the other predictions. However the difference between the predictions is small and acceptable as the potentials are constructed in quite different ways.

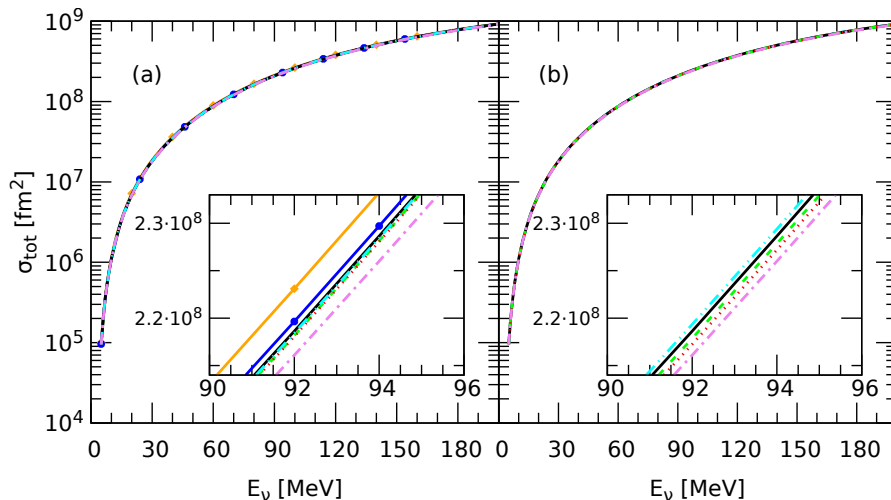


FIG. 9. The total cross section σ_{tot} for the $\nu_e + {}^2\text{H} \rightarrow \nu_e + p + n$ reaction as a function of the incoming neutrino energy in the laboratory system. The left panel (a) presents the dependence of σ_{tot} on the chiral order at $\Lambda = 450$ MeV. Dependence of σ_{tot} on the cutoff parameter value at $N^4\text{LO}$ is presented in panel (b). In the left panel the orange solid line with diamonds, the blue solid line with circles, the green dashed, red dotted, black solid, cyan double-dot-dashed and violet dot-dashed curves correspond to the LO, NLO, $N^2\text{LO}$, $N^3\text{LO}$, $N^4\text{LO}$, $N^4\text{LO}+$ and AV18 potential based predictions, respectively. In the right panel the cyan double-dot-dashed, black solid, green dashed, red dotted and violet dot-dashed curves represent results with $\Lambda = 400$ MeV, 450 MeV, 500 MeV, 550 MeV, and the AV18 based predictions respectively.

IV. ${}^3\text{HE}$ PHOTODISINTEGRATION

In this section we discuss predictions obtained when applying the chiral force with the semi-local regularization in momentum space to the ${}^3\text{He}$ photodisintegration process $\gamma + {}^3\text{He} \rightarrow p + p + n$. As in the ${}^2\text{H}$ case we use the Siegert theorem to go beyond the SNC approximation [25]. In the following we neglect the three-nucleon interaction. The semi-inclusive differential cross section $\frac{d^3\sigma}{d\Omega_p dE_p}$ for the photon laboratory energy $E_\gamma = 120$ MeV is presented in Fig. 12. Each of the four columns corresponds to a particular angle of the outgoing proton momentum with respect to the photon beam in the laboratory system (0° , 60° , 120° , and 180° , respectively). Top row shows the dependence of the predictions on the order of chiral expansion. As in Figs. 1, 7 and 8 we see that it is not enough to take into account only leading and next-to-leading orders to achieve convergence of the predictions and one has to include higher orders of chiral expansion. It is interesting to note that the older SCS potential seems to converge even faster as the NLO line in Fig. 12 is farther from the higher order curves than one in Fig. 9 of Ref. [13], where the predictions of the SCS chiral force for the same observable are shown. This is similar to the already observed picture for

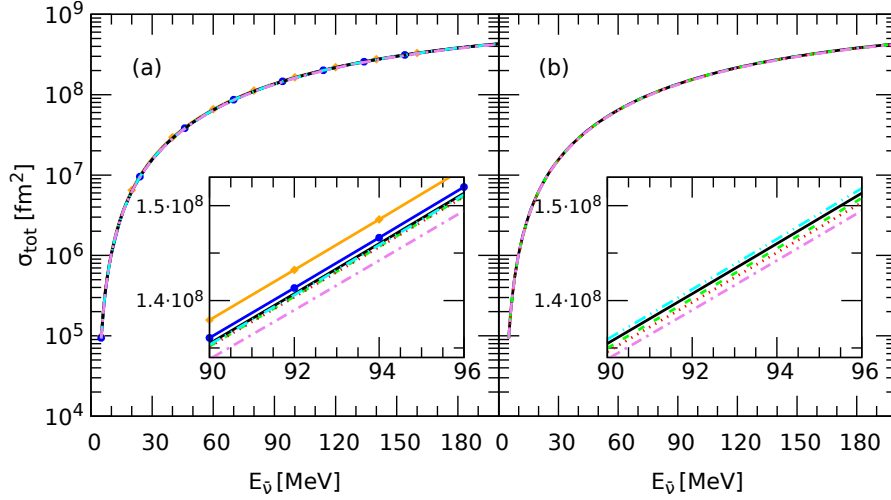


FIG. 10. Same as in Fig. 9 but for the $\bar{\nu}_e + {}^2\text{H} \rightarrow \bar{\nu}_e + \text{p} + \text{n}$ reaction.

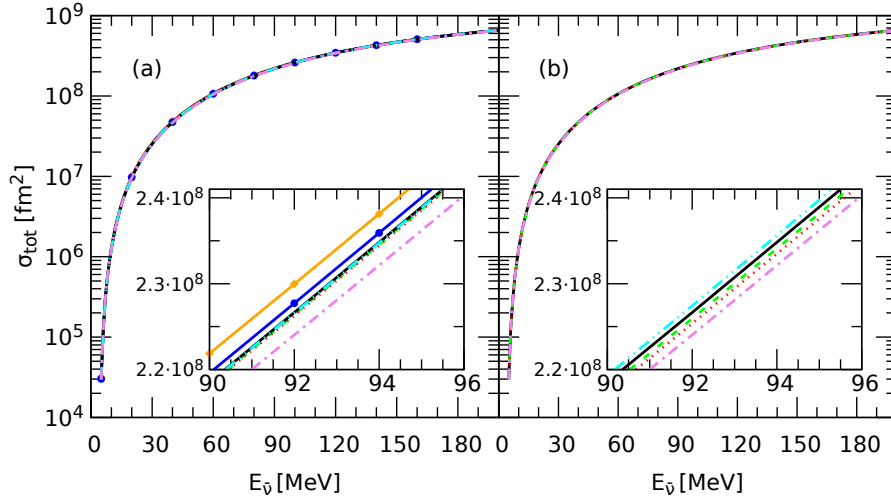


FIG. 11. Same as in Fig. 9 but for the $\bar{\nu}_e + {}^2\text{H} \rightarrow e^+ + \text{n} + \text{n}$ reaction.

the deuteron photodisintegration.

The bottom row represents the cutoff dependence of the cross section which proves to be weak. For most of the proton energies the maximum difference between all predictions remains below 10%. There are only exceptions for the outgoing proton angle 0° and its energies greater than 80 MeV, where the difference amounts to 20% and for the angle 180° at the proton energies around 40 MeV, where it reaches 12%. The cut-off dependence revealed by the SMS chiral force is weaker than it is observed for the SCS force (compare Fig. 11 in Ref. [13]).

The five-fold differential cross section $\frac{d^5\sigma}{d\Omega_1 d\Omega_2 dS}$ for the same process is presented in Fig. 13 for the photon laboratory energy $E_\gamma = 40$ MeV for two protons detected at the following polar

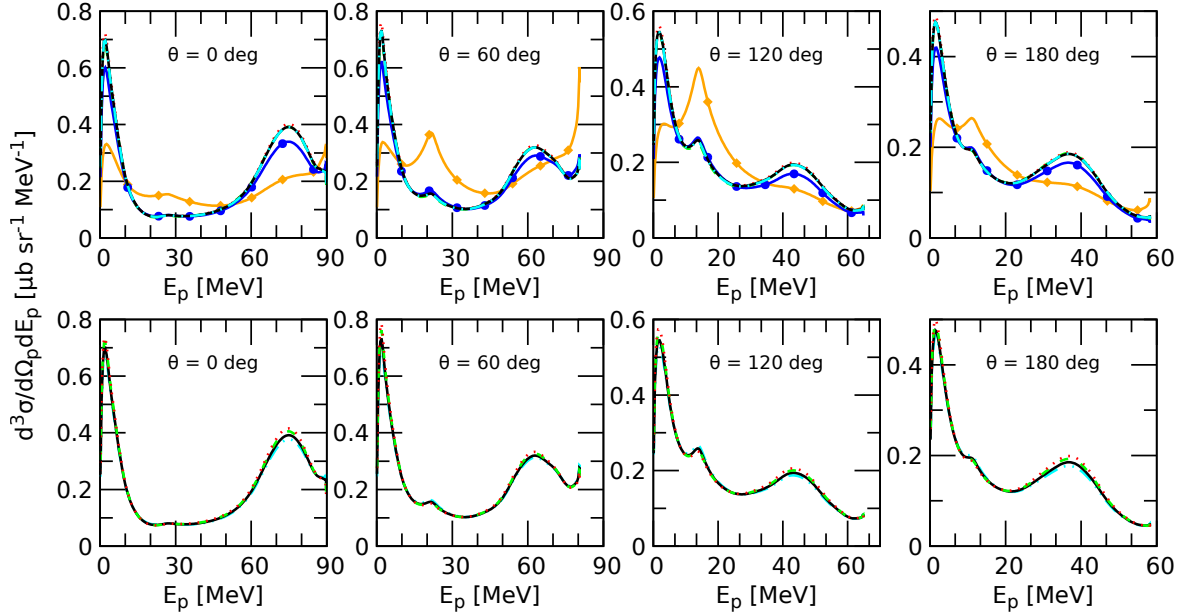


FIG. 12. The semi-inclusive differential cross section $\frac{d^3\sigma}{d\Omega_p dE_p}$ for the $\gamma + {}^3\text{He} \rightarrow p + p + n$ reaction at $E_\gamma = 120$ MeV as a function of the outgoing proton energy E_p at different values of the polar angle of the outgoing proton momentum θ_p . Top row shows the cross section dependence on the order of chiral expansion (at $\Lambda = 450$ MeV), the bottom row shows the dependence on the value of the cutoff parameter Λ . The curves are as in Fig. 1 but the AV18 prediction is not shown here.

and azimuthal angles (assuming that the momentum of the initial photon \vec{p}_γ is parallel to the z -axis) $\Theta_1 = 15^\circ$, $\Phi_1 = 0^\circ$ and $\Theta_2 = 15^\circ$, $\Phi_2 = 180^\circ$. The arc-length S of the kinematical locus in the $E_1 - E_2$ plane, where E_1 and E_2 are the kinetic energies of the two detected nucleons, is used to uniquely define the kinematics of the three-body breakup reaction [41]. We observe that the NLO contribution is very important since it raises the LO cross section by a factor of two. An additional shift (around 9%) comes from $N^2\text{LO}$ and only small changes are seen when $N^3\text{LO}$, $N^4\text{LO}$ and $N^4\text{LO}^+$ force components are included. However, even for the highest orders ($N^4\text{LO}$ and $N^4\text{LO}^+$) curves do not overlap, which suggests that full convergence is not achieved yet. With respect to the cut-off dependence the picture is more stable, since it is very hard to distinguish individual predictions in the right panel.

Figure 14 shows the cross section for the same choice of polar and azimuthal angles as presented in Fig. 13 but for the higher incoming photon energy $E_\gamma = 120$ MeV. The general trends do not change with increasing energy, except for the fact that the dependence on the regularization parameter is slightly stronger which is visible at the maxima of the cross sections around $S=15$ MeV and $S=100$ MeV. But for all other values of the arc-length parameter S almost full agreement between all the lines exists.

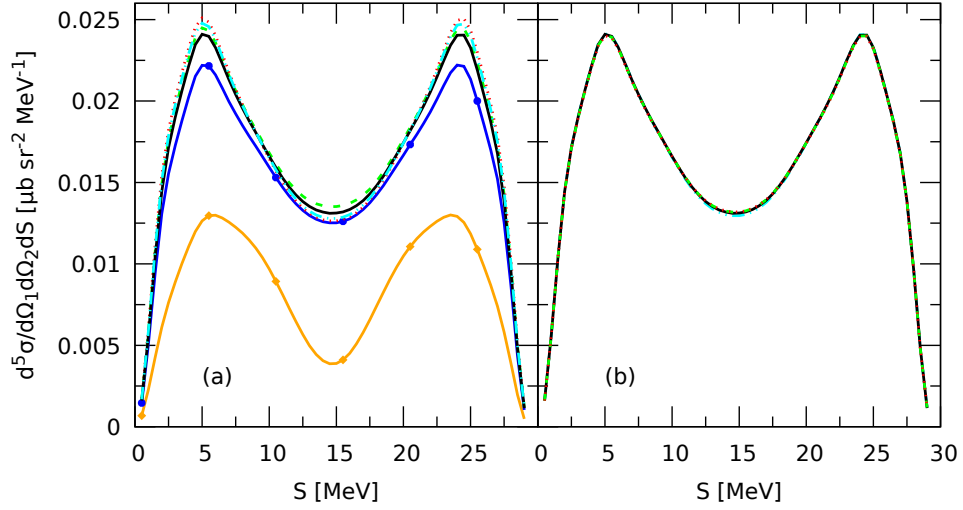


FIG. 13. The five-fold differential cross sections $\frac{d^5\sigma}{d\Omega_1 d\Omega_2 dS}$ for the complete kinematical configuration with the two protons detected at $\Theta_1 = 15^\circ$, $\Phi_1 = 0^\circ$, $\Theta_2 = 15^\circ$, $\Phi_2 = 180^\circ$ angles for the ${}^3\text{He}$ photodisintegration process at the photon energy $E_\gamma = 40$ MeV in the laboratory frame. The dependence on the chiral order (with $\Lambda = 450$ MeV) is presented in the left panel (a) and the results for different cutoff values (at $N^4\text{LO}$) are displayed in the right one (b). Curves are as in Fig.12.

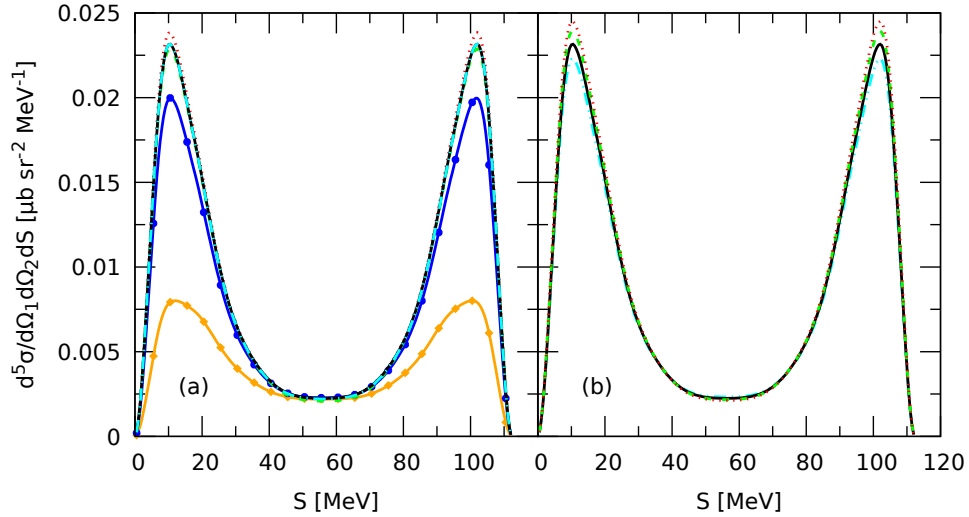


FIG. 14. Same as in Fig. 13 but for $E_\gamma = 120$ MeV.

V. SUMMARY AND CONCLUSIONS

We presented the results of the application of the chiral NN potential with the semi-local regularization in momentum space to a number of electroweak reactions: the ${}^2\text{H}$ and ${}^3\text{He}$ photodisintegrations and the (anti)neutrino induced deuteron breakup reactions: $\gamma + {}^2\text{H} \rightarrow$

$p + n, \gamma + {}^3\text{He} \rightarrow p + p + n, \nu_e + {}^2\text{H} \rightarrow \nu_e + p + n, \bar{\nu}_e + {}^2\text{H} \rightarrow \bar{\nu}_e + p + n$ and $\bar{\nu}_e + {}^2\text{H} \rightarrow e^+ + n + n$. In the case of the ${}^3\text{He}$ photodisintegration we focus on the properties of the applied NN potential and neglect the three-body force.

All our results show a weaker, compared to the previous version of the Bochum-Bonn chiral potential (the SCS force), dependence on the cutoff parameter Λ . A small spread of results obtained with different values of Λ make the predictions based on the current interaction model more unambiguous. We also observe good convergence of the predictions with respect to the chiral order and the possibility to include some terms from the sixth order (N^4LO^+) favorably distinguishes the SMS force from the SCS one.

As we have no full 2N electromagnetic current consistent with the SMS interaction at our disposal, the Siegert theorem was used to take two-nucleon contributions in the electromagnetic current operator at least partly into account for the photodisintegration processes. As a consequence, the incomplete electromagnetic current operator leads to some problems with the data description, as seen in Fig. 1. We expect that future application of the electromagnetic current operator fully consistent with the 2N potential will significantly improve the agreement with the data.

The presented polarization observables for the deuteron photodisintegration processes (A_X and P_y) are the ones, where the slowest convergence with respect to the chiral order and the strongest dependence on the regularization parameter is noticed. For instance for the deuteron analyzing powers (T_{11}, T_{20}, T_{21} and T_{22}) the convergence is very fast (above the leading order) and the cutoff variation is negligible.

The same picture is also valid for the investigated here total cross sections for the weak ${}^2\text{H}$ disintegrations via neutral or charged currents: the convergence with respect to the chiral order is quite rapid and the cutoff dependence is weak.

The new SMS potential has a number of practical advantages in comparison to the older chiral forces. Its predictions show weaker dependence on the cut-off parameter and good convergence with respect to the order of chiral NN potential. There is still room for improvement in our calculations. The main drawback of the present formalism is the lack of the explicit electroweak current operator entirely consistent with the 2N SMS interaction as well as the omission of the three-nucleon force for the ${}^3\text{He}$ disintegration. In addition, the future complete studies should be supplemented with an analysis of truncation errors using the Bayesian approach, which would allow one to draw more reliable conclusions about the convergence pattern of chiral EFT predictions for these reactions. Nevertheless, our results with the simplified Hamiltonian reveal the usefulness of the SMS chiral force for studies of various electroweak processes in few-nucleon systems in the near future.

VI. ACKNOWLEDGEMENTS

This work is a part of the LENPIC project and was supported by the Polish National Science Center under Grants No. 2016/22/M/ST2/00173 and 2016/21/D/ST2/01120. It was also supported in part by BMBF (Grant No. 05P18PCFP1) and by DFG through funds provided to the Sino-German CRC 110 Symmetries and the Emergence of Structure in QCD (Grant No. TRR110). The numerical calculations were partially performed on the

supercomputer cluster of the JSC, Jülich, Germany.

- [1] P. Reinert, H. Krebs, and E. Epelbaum, *Eur. Phys. J. A* **54**, 86 (2018).
- [2] E. Epelbaum, H.-W. Hammer, and Ulf-G. Meißner, *Rev. Mod. Phys.* **81**, 1773 (2009).
- [3] R. Machleidt and D. R. Entem, *Phys. Rept.* **503**, 1 (2011).
- [4] M. Piarulli, L. Girlanda, L. E. Marcucci, S. Pastore, R. Schiavilla, and M. Viviani, *Phys. Rev. C* **87**, 014006 (2013).
- [5] E. Epelbaum, H. Krebs, and U.-G. Meißner, *Phys. Rev. Lett.* **115**, 122301 (2015).
- [6] V. Bernard, E. Epelbaum, H. Krebs, and Ulf-G. Meißner, *Phys. Rev. C* **77**, 064004 (2008).
- [7] V. Bernard, E. Epelbaum, H. Krebs, and Ulf-G. Meißner, *Phys. Rev. C* **84**, 054001 (2011).
- [8] E. Epelbaum, J. Golak, K. Hebeler, H. Kamada, H. Krebs, U.-G. Meißner, A. Nogga, P. Reinert, R. Skibiński, K. Topolnicki, Yu. Volkotrub, and H. Witała, *Eur. Phys. J. A* **56**, 92 (2020).
- [9] Yu. Volkotrub, J. Golak, R. Skibinski, K. Topolnicki, H. Witała, E. Epelbaum, H. Krebs, and P. Reinert, *Journal of Physics G: Nuclear and Particle Physics* (2020).
- [10] R. Skibiński, J. Golak, H. Witała, W. Glöckle, A. Nogga, and E. Epelbaum, *Acta Phys. Polon. B* **37**, 2905 (2006).
- [11] R. Skibiński, J. Golak, D. Rozpędzik, K. Topolnicki, and H. Witała, *Acta Phys. Polon. B* **46**, 159 (2015).
- [12] D. Rozpędzik, J. Golak, S. Kölling, E. Epelbaum, R. Skibiński, H. Witała, and H. Krebs, *Phys. Rev. C* **83**, 064004 (2011).
- [13] R. Skibiński, J. Golak, K. Topolnicki, H. Witała, E. Epelbaum, H. Kamada, H. Krebs, Ulf-G. Meißner, and A. Nogga, *Phys. Rev. C* **93**, 064002 (2016).
- [14] E. Epelbaum, H. Krebs, and U.-G. Meißner, *Eur. Phys. J. A* **51**, 53 (2015).
- [15] R. B. Wiringa, V. G. J. Stoks, and R. Schiavilla, *Phys. Rev. C* **51**, 38 (1995).
- [16] E. Epelbaum, H. Krebs, and P. Reinert, *Front. in Phys.* **8**, 98 (2020).
- [17] D. Riska and G. Brown, *Phys. Lett. B* **38**, 193 (1972).
- [18] D. O. Riska, *Phys. Scr.* **31**, 107 (1985); **31**, 471 (1985).
- [19] J. Carlson and R. Schiavilla, *Rev. Mod. Phys.* **70**, 743 (1998).
- [20] H. Arenhövel and M. Schwamb, *Eur. Phys. J. A.* **12**, 207 (2001).
- [21] L. E. Marcucci, M. Viviani, R. Schiavilla, A. Kievsky, and S. Rosati, *Phys. Rev. C* **72**, 014001 (2005).
- [22] S. Kölling, E. Epelbaum, H. Krebs, and U.-G. Meißner, *Phys. Rev. C* **84**, 054008 (2011).
- [23] A. Baroni and R. Schiavilla, *Phys. Rev. C* **96**, 014002 (2017).
- [24] A. A. Filin, V. Baru, E. Epelbaum, H. Krebs, D. Möller, and P. Reinert, *Phys. Rev. Lett.* **124**, 082501 (2020).
- [25] J. Golak, R. Skibiński, H. Witała, W. Glöckle, A. Nogga, and H. Kamada, *Phys. Rept.* **415**, 89 (2005).
- [26] J. Golak, R. Skibiński, H. Witała, K. Topolnicki, A. E. Elmeshneb, H. Kamada, A. Nogga, and L. E. Marcucci, *Phys. Rev. C* **90**, 024001 (2014).
- [27] J. Golak, H. Kamada, H. Witała, W. Glöckle, J. Kuroś, R. Skibiński, V. V. Kotlyar, K. Sagara, and H. Akiyoshi, *Phys. Rev. C* **62**, 054005 (2000).
- [28] J. Golak, R. Skibiński, K. Topolnicki, H. Witała, A. Grassi, H. Kamada, and L. E. Marcucci, *Phys. Rev. C* **98**, 015501 (2018).

- [29] J. Golak, R. Skibiński, K. Topolnicki, H. Witała, A. Grassi, H. Kamada, and L. E. Marcucci, *Phys. Rev. C* **100**, 064003 (2019).
- [30] H. Krebs, *PoS CD2018*, 098 (2020).
- [31] S. Kölling, E. Epelbaum, H. Krebs, and U.-G. Meißner, *Phys. Rev. C* **80**, 045502 (2009).
- [32] H. Krebs, E. Epelbaum, and U.-G. Meißner, *Annals Phys.* **378**, 317 (2017).
- [33] H. Krebs, E. Epelbaum, and U.-G. Meißner, *Few Body Syst.* **60**, 31 (2019).
- [34] H. Krebs, E. Epelbaum, and Ulf-G. Meißner, (2020), arXiv:2005.07433 [nucl-th].
- [35] H. Arenhövel and M. Sanzone, *Few Body Syst. Suppl.* **3** (1991).
- [36] S. Binder *et al.* (LENPIC), *Phys. Rev. C* **93**, 044002 (2016).
- [37] R. J. Furnstahl, N. Klco, D. R. Phillips, and S. Wesolowski, *Phys. Rev. C* **92**, 024005 (2015).
- [38] S. Q. Ying, E. M. Henley, and G. A. Miller, *Phys. Rev. C* **38**, 1584 (1988), *and references therein*.
- [39] E. De Sanctis *et al.*, *Phys. Rev. Lett.* **54**, 1639 (1985).
- [40] S. Binder, A. Calci, E. Epelbaum, R. J. Furnstahl, J. Golak, K. Hebeler, T. Hüther, H. Kamada, H. Krebs, P. Maris, Ulf-G. Meißner, A. Nogga, R. Roth, R. Skibiński, K. Topolnicki, J. P. Vary, K. Vobig, and H. Witała (LENPIC Collaboration), *Phys. Rev. C* **98**, 014002 (2018).
- [41] W. Glöckle, H. Witała, D. Hüber, H. Kamada, and J. Golak, *Phys. Rept.* **274**, 107 (1996).